Multi-scale quantum point contact model for filamentary conduction in resistive random access memories devices

Xiaojuan Lian,[1,a)] Xavier Cartoixà,[1] Enrique Miranda,[1] Luca Perniola,[2] Riccardo Rurali,[3] Shibing Long,[4] Ming Liu,[4] and Jordi Suñé[1]
[1]*Departament d'Enginyeria Electrònica, Universitat Autònoma de Barcelona, 08193 Bellaterra, Spain*
[2]*CEA-LETI, MINATEC, Grenoble, France*
[3]*Institut de Ciència de Materials de Barcelona (ICMAB-CSIC), Campus de Bellaterra, 08193 Bellaterra, Spain*
[4]*Laboratory of Nanofabrication and Novel Device Integration, Institute of Microelectronics, Chinese Academy of Sciences, Beijing 100029, China*

(Received 14 May 2014; accepted 12 June 2014; published online 25 June 2014)

We depart from first-principle simulations of electron transport along paths of oxygen vacancies in HfO_2 to reformulate the Quantum Point Contact (QPC) model in terms of a bundle of such vacancy paths. By doing this, the number of model parameters is reduced and a much clearer link between the microscopic structure of the conductive filament (CF) and its electrical properties can be provided. The new multi-scale QPC model is applied to two different HfO_2-based devices operated in the unipolar and bipolar resistive switching (RS) modes. Extraction of the QPC model parameters from a statistically significant number of CFs allows revealing significant structural differences in the CF of these two types of devices and RS modes. © *2014 AIP Publishing LLC*.
[http://dx.doi.org/10.1063/1.4885419]

I. INTRODUCTION

Resistive switching (RS) in metal-insulator-metal (MIM) or metal-insulator-semiconductor (MOS) devices is often based on the creation and partial destruction of a conductive filament (CF) of nanoscale dimensions.[1–10] Therefore, understanding the conduction properties of the CF in the Low-Resistance State (LRS) and the High-Resistance State (HRS)[11–17] and linking these properties to the shape and nature of the CF is of great importance to improve the understanding of RS and to boost Resistive Random Access Memories (RRAM) applications.

Many different conduction models have been proposed for the HRS including trap-assisted tunneling,[18] Poole–Frenkel conduction,[19] thermally activated hopping,[20] space-charge limited current,[21] and the Quantum Point Contact model (QPC),[22,23] among others. Although the results might somehow depend on the considered oxide material, in the case of HfO_2 there are strong experimental evidences supporting the importance of tunneling in the HRS.[18] On the other hand, the experimental evidence of a CF behaving as a Quantum Wire (QW) in the LRS has been reported in a variety of RRAM devices, including HfO_2-based structures.[24–29] The single model which provides a smooth transition from tunneling in the HRS to Ohmic conduction in the LRS and which naturally explains conductance quantization effect is the QPC model. This model is based on the idea that the CF can be modeled as a QW, and it has been successfully applied to model the conduction properties in RRAM both in the HRS and the LRS.[30–32]

The QPC model will be reformulated by coupling it to the results of first-principle simulations of oxygen vacancy paths. In this way, the number of model parameters is reduced and a much clearer link between the microscopic structure of the CF and its electrical properties can be provided. The multi-scale QPC model will be applied to two different HfO_2-based RRAM devices, Pt/HfO_2/Pt and Pt/Ti/HfO_2/Pt operated in the unipolar and bipolar RS modes.

II. THE THEORETICAL BASIS

A. First-principle simulation of HfO_2

Ab-initio calculations of the transport properties of metal/HfO_2/metal structures with paths of oxygen vacancies in hafnium oxide (Fig. 1(a)) have demonstrated the appearance of extended bands in the gap of HfO_2 (Fig. 1(b)).[27] Using a Green's function formalism coupled with a density functional theory code, the conductance of vacancy filaments of different width was calculated,[33–36] showing that even the narrowest filament (one vacancy path) can sustain a conductive channel, with conductance of the order of G_0.[37] On the other hand, as shown in Fig. 1(c), each time that a vacancy is removed from the single-vacancy filament, the conductance is reduced by a factor of ~10. Taking into account that the separation between vacancies is ~0.26 nm, the re-oxidation of a vacancy introduces a spatial gap in the filament which acts as a tunneling potential barrier of about this thickness. As a consequence, the conductance of the vacancy path (i.e., its barrier transmission coefficient) exponentially decreases with the gap thickness, $G = G_0 \exp(-t_{gap}/t_0)$ with $t_0 = 0.12$ nm, as shown in the Fig. 1(d).

Given these *ab-initio* results, the concept of CF narrowing is only meaningful when there are $N > 1$ vacancy paths. Further narrowing of the CF is not possible and the description of CF states with $G \ll G_0$ requires the existence of a spatial gap in the CF, i.e., at least one vacancy re-oxidized,

[a)]xjlian2005@gmail.com

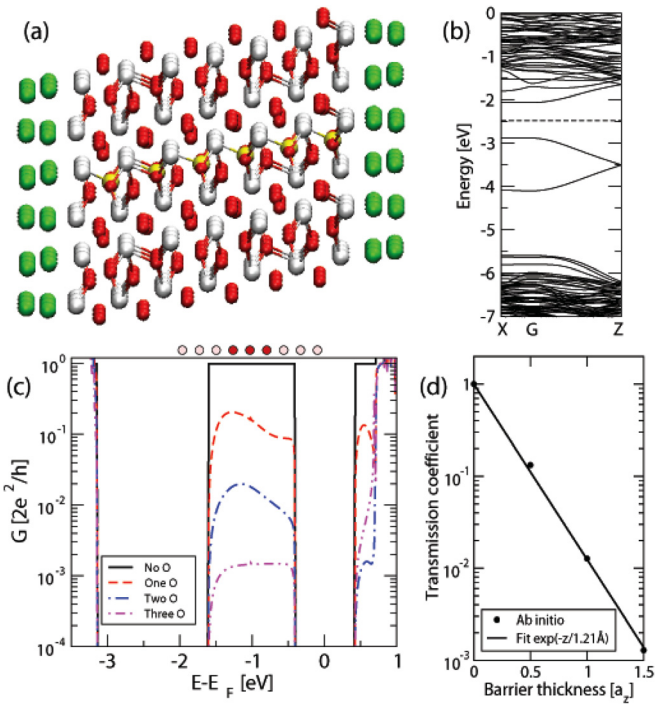

FIG. 1. (a) Schematic representation of a single vacancy path (yellow balls) in monoclinic HfO_2, with green/red/white balls indicating metal/oxygen/hafnium atoms, respectively. (b) Band structure for the configuration of Fig. 1(a), without the metallic contacts, showing that the vacancy path introduces an extended band in the HfO_2. (c) Conductance associated to the extended band in the gap. When the vacancy filament is complete, conductance is G_0 and it is strongly suppressed when 1, 2, or 3 vacancies are removed (substituted by an oxygen atom). (d) The transmission coefficient as a function of the barrier thickness (a_z is 0.52 nm, thus the separation between vacancies is ~0.26 nm) is reduced by a factor of ~10 when each vacancy is removed from the CF. Fitting line corresponds to $T = \exp(-t_{gap}/t_0)$ with $t_0 = 0.12$ nm.

which poses a potential barrier to electron transmission. Thus, the HRS will be described as a tunneling process through the CF gap, a process which is fully equivalent to that considered in Ref. 18.

B. The multi-scale QPC model coupled to *ab-initio* results

The QPC model is based on the Landauer transmission approach to conduction along narrow microscopic constrictions and it assumes that the CF is a quasi-one dimensional system of electron states.[38] The area of the most constrictive section of the CF determines the energy of the subbands available for transport along the CF. If the CF is wide, the position of this first subband is below the electrode Fermi level and the conduction is essentially linear with a conductance of the order of $G_0 = 2e^2/h$ or larger. On the contrary, if the CF is narrow, the energy of the first subband might be above the electrode Fermi level and this would introduce a potential barrier which, depending on its height and thickness, might result in a CF conductance several orders of magnitude below G_0 and strongly non-linear I-V. This basic modeling framework has been assumed by different groups with some small different details. Miranda[30] has considered a bundle of N of conducting single-subband CFs in the LRS and a single channel with a parabolic barrier in the HRS. Degraeve[31] described the filament as a saddle potential energy surface and extracted the model parameters from many reset I-V curves, thus providing evidence that the dominant microscopic evolution of the CF during reset consists in the progressive narrowing of the constriction. However, in this paper, we will keep the structure of Miranda's formulation of the QPC model.

According to the Landauer's approach, the current flowing through a CF with N vacancy paths can be calculated as[39]

$$I(V) = \frac{2e}{h} N \int_{-\infty}^{\infty} T(E)\{ f(E - \beta eV) - f(E + (1-\beta)eV)\} dE, \quad (1)$$

where E is the energy, $T(E)$ is the transmission probability, f is the Fermi-Dirac distribution function, e and h are the electron charge and the Planck constant, and V is the applied voltage which is assumed to drop at the cathode and anode interfaces with the QPC in a fraction of β and $(1-\beta)$, respectively (Fig. 2).

Assuming an inverted parabolic potential barrier allows to obtain an analytical expression for the tunneling probability,[40–42] $T(E) = \{1 + \exp[-\alpha(E-\Phi)]\}^{-1}$, where Φ is the barrier height and $\alpha = t_B \pi^2 h^{-1} \sqrt{2m^*/\Phi}$ is related to the inverse of potential barrier curvature, m^* is the effective electron mass and t_B is the barrier thickness at the equilibrium Fermi energy, assumed to be equal to t_{gap}. Inserting the transmission coefficient into Eq. (1)

$$I = \frac{2e}{h} N \left\{ eV + \frac{1}{\alpha} Ln \left[\frac{1 + \exp\{\alpha[\Phi - \beta eV]\}}{1 + \exp\{\alpha[\Phi + (1-\beta)eV]\}} \right] \right\}. \quad (2)$$

This equation can be applicable to both the HRS and the LRS depending on the values of α and Φ, which describe the potential barrier. If there is a gap with a potential barrier, this equation is found to converge to $I \approx NG_0 \exp(-\alpha\Phi)V$ at low voltages so that the equivalent transmission probability is $T = \exp(-\alpha\Phi)$. Linking this to the thickness dependence obtained from the *ab-initio* results $T = \exp(-t_{gap}/t_0)$, we can obtain that $t_{gap} = t_0 \alpha \Phi$ and $\Phi = 2\hbar^2/m^* \pi^2 t_0^2$. Assuming that $m^* \sim m_0$ (our *ab-initio* calculations give $m^* = 1.08\, m_0$ at the bottom of the one-vacancy electron band) results in a barrier height $\Phi \sim 1.16$ eV, which is a perfectly consistent value, given the large gap of HfO_2. In any case, other values of m^* down to $\sim 0.5\, m_0$ would give reasonable values of Φ below 2.5 eV and will not significantly affect the quality of

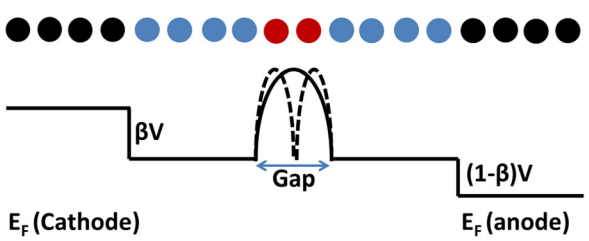

FIG. 2. Schematic representation of a single vacancy path with two re-oxidized vacancies and the associated voltage profile under bias.

the fit of the experimental I-V characteristics nor the extracted information about the microscopic structure of the CF. On the other hand, the extracted value of the gap thickness (from the same set of experimental results) would also increase by a factor of 2 because of $t_{gap} \sim \Phi \sim 1/m^*$. Since the extracted values of gap thickness are very small as compared to the thickness of the insulator, even if we had to multiply them by a factor of 2 or larger, these values would still be reasonable. Finally, let us comment that in the limit that there is no spatial gap, Eq. (2) converges to $I = NG_0V$, a linear I-V which is consistent with what is usually observed in the LRS. When the CF is relatively narrow (small N), this equation explains the experimentally reported conductance quantization effects. For large values of N, the model approaches the classical Ohmic regime, where quantization becomes less evident because of the large values of CF conductance.

After reformulating the QPC model by coupling it to the results of *ab-initio* simulations of oxygen vacancy paths, only three free fitting parameters remain: the number of vacancy paths N (i.e., the lateral size of the CF) with the constraint $N \geq 1$, the average t_{gap} in these paths (for simplicity all the paths are assumed to be identical) and the average value of the asymmetry parameter β, with the constraint $0 < \beta \leq 1$. However, in order to simplify the fitting process, we will usually assume a fixed value of β and extract only N and t_{gap} from the experimental data using Least-square-estimation (LSE) method.

In the following sections, experimental results are fit to the new multi-scale QPC model and the statistics of model parameters is reported. Fixing $\Phi = 1.16\,\text{eV}$ and $\beta = 0.5$ (symmetry) or $\beta = 1$ (asymmetry), we use Eq. (2) to fit the experimental I-V curves in HRS and LRS for HfO_2-based RRAM devices to get the values of N and α (t_{gap}). Finally, some indirect information about the microscopic structure of the CF will be discussed using the extracted QPC parameters and their evolution during set and reset transitions.

III. RESULTS AND DISCUSSION

Cycling experiments consisting of 1250 consecutive set/reset operations have been performed using the ramp voltage sweep (RVS) method in two different HfO_2-based RRAM structures, as shown in our recent paper.[29] In particular, we will study RS in Pt/HfO_2/Pt operated in the unipolar mode (same polarity for set and reset) and Pt/Ti/HfO_2/Pt structures operated under unipolar and bipolar switching modes. The considered structures are 2.5 μm^2 MIM capacitors fabricated in a mesa structure on top of a tungsten plug. The insulator is a 10-nm-thick HfO_2 layer deposited by atomic layer deposition (ALD) at 350 °C on top of the Pt bottom electrode (BE), followed by Pt (or Pt/Ti) top electrode (TE) deposition and patterning. BE and TE were deposited by physical vapor deposition (PVD). Electrical stress and measurements have been performed at the wafer level with a Keithley 4200SCS Semiconductor Characterization System. To initiate the RS behavior, an electroforming process is required to generate the CF. In all the cases, electroforming has been achieved by application of a voltage ramp with a current compliance of 1 mA (imposed by the measuring apparatus) so as to avoid the occurrence of hard breakdown, which would cause the device failure and impede any ulterior observation of RS. This compliance limit is also kept during each set cycle. During the reset voltage ramp, the current is allowed to flow without external limit.

A. Nonpolar Pt/HfO_2/Pt devices

The Pt/HfO_2/Pt devices are symmetric structures which show nonpolar RS, this means that Pt/HfO_2/Pt devices can be set or reset by any combination of voltage bias (positive/positive; negative/negative, positive/negative, and vice versa). In all these operating modes, the RS phenomenology is very similar but the results considered in this paper correspond to unipolar RS mode, i.e., a positive bias voltage ramp is applied both for set and for reset. After each reset cycle and after each set cycle, the new QPC model parameters are extracted by the least-square fitting of I-V curves so as to get statistical information about the CF in the HRS and in the LRS. Notice that we focus on cycle-to-cycle variations of the CF and not on sample-to-sample variations. The CF conductance at low voltage is calculated by $R_{CF} = I/V$ at $V = 0.1$ V and a histogram of its distribution is shown in Fig. 3(a). In the LRS, the CF conductance peak is located at $\sim 100G_0$, while after reset two peaks of CF conductance are found: one narrow peak located between G_0 and $5G_0$ and a wide peak spanning from $10^{-5}G_0$ to $10^{-1}G_0$. In the LRS, the I-V curves are roughly linear with a small deviation from linearity at high currents, probably due to temperature dependent conductivity.[43] The QPC model can also be applied to the LRS ($I \approx N\beta G_0 V$ in this limit) although the CF conductance is so large that the CF behaves essentially as a classical metallic wire. In this limit, the extracted number of conducting channels can be interpreted as being proportional to the area of the CF constriction.

The analysis of the properties of the CF in the HRS for Pt/HfO_2/Pt structures provides enough useful information. As shown in Figs. 3(a) and 3(b), the HRS includes values of CF conductance spanning from slightly above G_0 down to $10^{-5}G_0$. A perfect I-V fitting is obtained in more than 5 orders of magnitude of conductance. When the CF conductance is of the order of G_0 or higher, the I-V is found to be linear, consistent with the idea that one or several oxygen vacancy paths connect the two electrodes through extended quasi-one dimensional electron subbands. For less conducting CFs, the I-V is found to be non-linear as the bias voltage increases. In general, the non-linearity increases with decreasing CF conductance and this corresponds to the tunneling regime. Figs. 3(c) and 3(d) show the extracted QPC model parameters which are only N and t_{gap} because $\beta = 0.5$ has been assumed for this structure and switching mode. This choice improves the quality of the I-V fitting and it is consistent with the symmetry of this RRAM structure. As shown in Fig. 3(c), for CF conductance below G_0, the best fit is obtained for $N = 1$, while for $G > G_0$ the number of conducting channels perfectly correlates with the CF conductance. On the other hand, Fig. 3(d) shows that there is no potential barrier for $G > G_0$ (i.e., $t_{gap} = 0$), and the

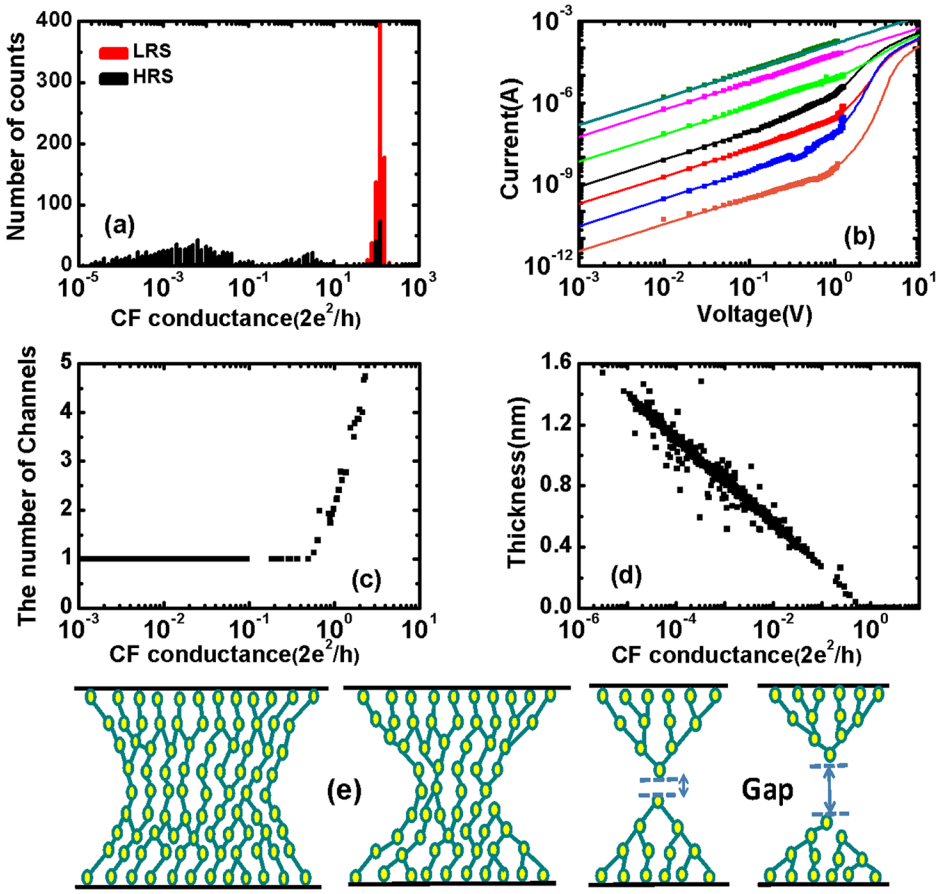

FIG. 3. Nonpolar switching in Pt/HfO_2/Pt structures. (a) Histogram of conductance at 0.1 V after set (red) and reset (black) cycles for 1250 successive set/reset cycles. (b) Examples of fitting of the I-V characteristics in the HRS. The CF conductance ranges from $G = 3.9e^{-5}G_0$ to $G \sim 2G_0$. Extracted QPC model parameters: (c) number of conducting channels, i.e., number of single vacancy paths (N) versus CF conductance; and (d) thickness of the gap (t_{gap}) versus CF conductance. (e) Schematic representation of the CF structure evolution from the LRS to the HRS.

thickness of the gap shows a perfect exponential correlation with the CF conductance below G_0, as expected for tunneling through a potential barrier. Thus, we conclude that below G_0, the CF has a very narrow constriction (likely one single oxygen vacancy path wide) with a spatial gap that ranges from 0 to 1.4 nm. This thickness range indicates that the gap can be estimated to be of up to ~6 re-oxidized vacancies in the least conductive CFs. Given that the CF conductance in the LRS is of the order of 10^2G_0, the conductance ratio of LRS to HRS can be as large as 10^7. This large change is achieved by combining the narrowing of the CF from ~267 vacancy paths (in the LRS) to one single path followed by the opening of a gap. Although the change of conductance is very large, it is concluded that the gap thickness (<1.4 nm) is only a small portion of the total CF length (10 nm). The long CF stumps that remain after each reset cycle explain why the spatial location of the CF likely remains the same along the very large number of set/reset cycles. This is because the probability of generating new CFs in different locations is much less favorable than the CF rejuvenation during the successive set cycles. According to the previous results, the evolution of the geometry of the CF from the LRS to the HRS is schematically depicted in Fig. 3(e). Starting from a very wide CF in the LRS, the first stage of the reset process consists in the reduction of the width of the CF in its most constrictive part to a limit in which only one or few oxygen vacancy paths connect the electrodes. This stage is followed by the opening of a gap, i.e., re-oxidation of one or several vacancies in all the paths. Once a gap is opened, the finding of $N = 1$ for $G < G_0$ means that the most conductive path controls the HRS I-V. In this regime (HRS), the thickness of the gap of the most conductive single vacancy path determines the CF conductance. In Fig. 3(e), we have assumed that the gap is in the center of the CF because the reset of these structures is likely due to thermal-enhanced dissolution and the center is likely the point of maximum temperature.[44]

B. Bipolar Pt/Ti/HfO_2/Pt devices

In Secs. III B and III C, the conductive properties of the CF in Pt/Ti/HfO_2/Pt devices will be analyzed. The structures include a thin Ti layer between the top Pt electrode and the HfO_2 layer. The Ti film is believed to act as an oxygen extraction layer and to introduce a high density of oxygen vacancies in the HfO_2. The vacancy profile is thought to be rather asymmetric with a much higher concentration near the top interface. As a consequence, when a CF is created during forming, its shape is expected to be highly asymmetric, with the narrowest constriction near the bottom interface. In fact, due to this asymmetry, these structures only show reliable RS operation when negative bias is applied to the top electrode for reset. In other words, in agreement with previous works, RS is only possible by re-oxidation of the tip of the CF, i.e., when the bottom electrode is the reset anode.[45] Thus, these devices can be operated under two different RS modes: unipolar (negative set/negative reset) and bipolar (positive set/negative reset), provided that reset is achieved

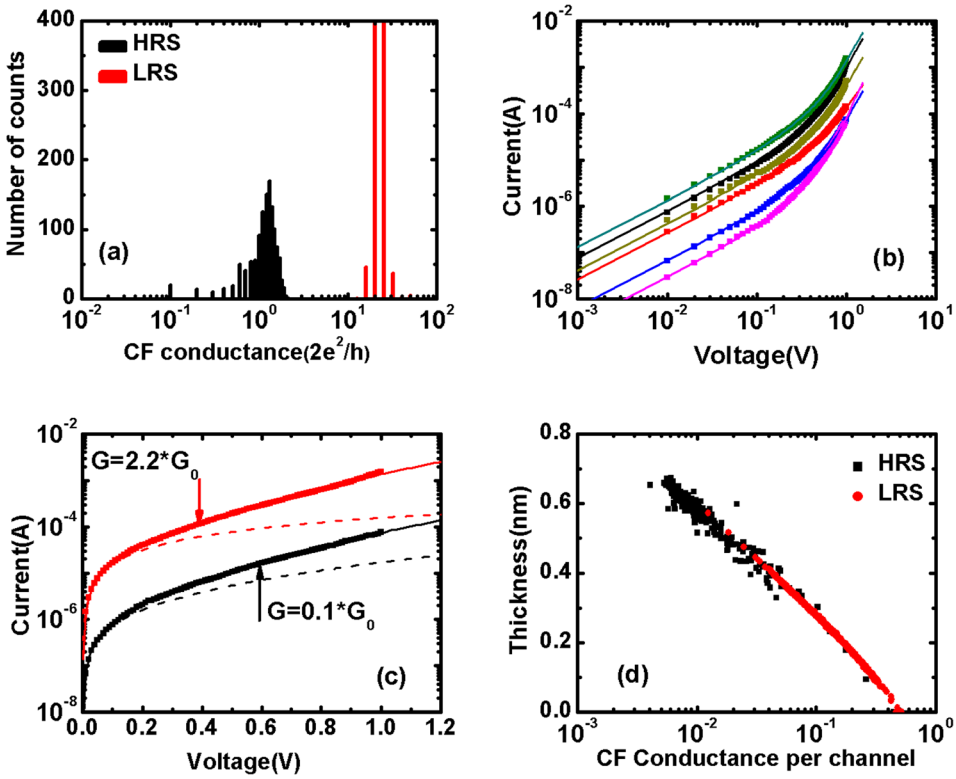

FIG. 4. Application of the QPC model to Pt/Ti/HfO_2/Pt structures operated under bipolar RS conditions. (a) Distribution of CF conductance measured at 0.1 V in the LRS (red) and HRS (black) during bipolar cycling experiment. (b) Fitting of I (V) to the QPC model in the HRS. (c) Demonstration that fitting with N = 1 (dashed black line) is not possible for low conductance CFs ($0.1G_0$) in the HRS nor it is possible to fit the I-V assuming linear conduction for $G > G_0$ (red dashed line) in the LRS. (d) Statistics of extracted QPC model parameters extracted from the fitting of 1250 I-V curves after the reset RVS in bipolar RS modes: gap thickness versus conductance per channel.

under negative polarity. Therefore, the properties of the CF in Pt/Ti/HfO_2/Pt devices, both under bipolar and unipolar RS operating are analyzed in the following sections.

Fig. 4(a) shows the histograms of CF conductance in the LRS and the HRS. In the case of Pt/HfO_2/Pt structures, the I-V in the LRS is essentially linear with a high voltage sub-linear behavior likely related to temperature-dependent conductivity. However, in this bipolar switching experiment, the CF conductance in the LRS is smaller ($\sim 30G_0$) although the compliance current during forming and set was kept at the same value (1 mA). In the HRS, the CF conductance is found to be in the range between $5e^{-2}G_0$ and $2G_0$, i.e., the bipolar reset is much less effective than the unipolar one in the Pt/HfO_2/Pt structures, and hence, the resistance ratio of the HRS and the LRS is much degraded, as usually found for bipolar RS. Other significant differences are that, as shown in Fig. 4(b), all the I-V curves after reset are significantly nonlinear in spite of the CF conductance being close or above to G_0. On the other hand, the nonlinearity is roughly independent of the CF conductance (the curves appear as almost parallel in the log-log plot). The fitting of the I-V curves to the QPC model is excellent, but the linear fit is not possible when $G > G_0$ nor it is possible to assume $N = 1$ for $G < G_0$, as explicitly shown in Fig. 4(c). In this particular case, the extraction of the QPC parameters (N and t_{gap}) was done under the assumption that $\beta = 1$. This value gives the best fitting results and is consistent with the strong asymmetry of the CF shape in structures which contain an oxygen extraction layer. Fig. 4(d) shows that the average gap thickness per conducting mode is found to converge to zero for $G/N \sim G_0$, as required by the QPC model.

Fig. 5(a) shows the extracted gap thickness versus CF conductance in the HRS and the LRS. We can see the average gap thickness is 0.59 nm in the HRS and 0.25 nm in the LRS; this is to say, there are about two or three re-oxidized vacancies in the HRS and one re-oxidized vacancy in the LRS. The number of CF paths versus conductance is shown in Fig. 5(b), which is different from what was found in the case of Pt/HfO_2/Pt structures. Many conduction paths are found to be active in the HRS but they show a gap with an average thickness corresponding to two or three vacancies. The average number of channels in the HRS and LRS is 134 and 192, respectively. According to the results of our analysis of properties by means of the reformulated QPC model, we can describe the evolution of the CF from the LRS to the HRS as shown in Fig. 5(c). Due to the asymmetry of the Pt/Ti/HfO_2/Pt structure, the CF is deduced to be conical with the tip contacting the bottom electrode being the active region during switching. In the LRS, the CF area is rather large (though smaller than in Pt/HfO_2/Pt structures) and there is one re-oxidized vacancy gap. In the HRS, and after a stabilization period of about 100 initial cycles, there is an average gap with the thickness of two or three vacancies and the CF conductance is modulated mainly by the area of the active CF tip.

C. Unipolar Pt/Ti/HfO_2/Pt devices

The experimental results of Pt/Ti/HfO_2/Pt devices in unipolar RS mode are different from bipolar RS mode, although the extraction of the QPC parameters (N and t_{gap}) was done under the assumption that $\beta = 1$ and $\Phi = 1.16$ eV. The CF conductance in the LRS ($\sim 30G_0$) is

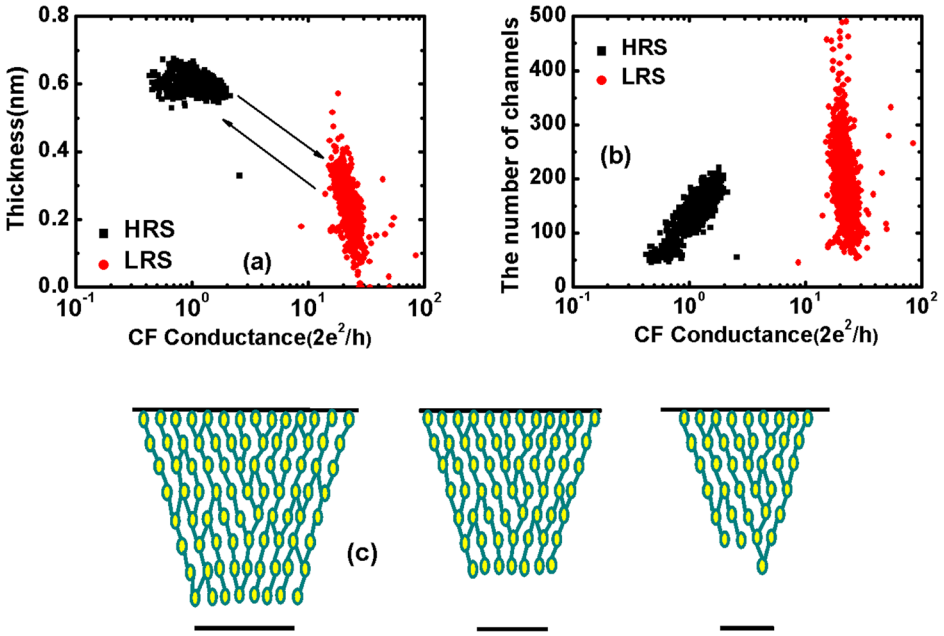

FIG. 5. Statistics of extracted QPC model parameters extracted from the fitting of 1250 I-V curves after the reset RVS in bipolar RS modes. (a) Thickness of the gap versus CF conductance in the HRS and the LRS. (b) The number of conducting channels versus CF conductance both in the HRS and the LRS. (c) Schematic representation of CF structure in bipolar experiments.

similar to bipolar RS mode while in the HRS, the CF conductance is smaller than bipolar RS mode, which is found to be in the range between $10^{-2}G_0$ and $4G_0$, that is to say, the unipolar RS mode is more effective than bipolar RS mode for Pt/Ti/HfO_2/Pt devices, but it is much less effective than Pt /HfO_2/Pt devices. Fig. 6(a) shows the excellent I-V fitting in the HRS using LSE method. When the CF conductance is of the order of G_0 or higher, the I-V tends to be linear, consistent with the idea that one or several oxygen vacancy paths connect the two electrodes through extended quasi-one dimensional electron subbands. Figs. 6(b)–6(d) show the extracted QPC parameters versus CF conductance. The average gap thickness is about 0.09 nm in the LRS and 0.356 nm in the HRS and the average gap thickness per conducting mode is found to converge to zero for $G/N \sim G_0$, as required by the QPC model. The average number of paths is about

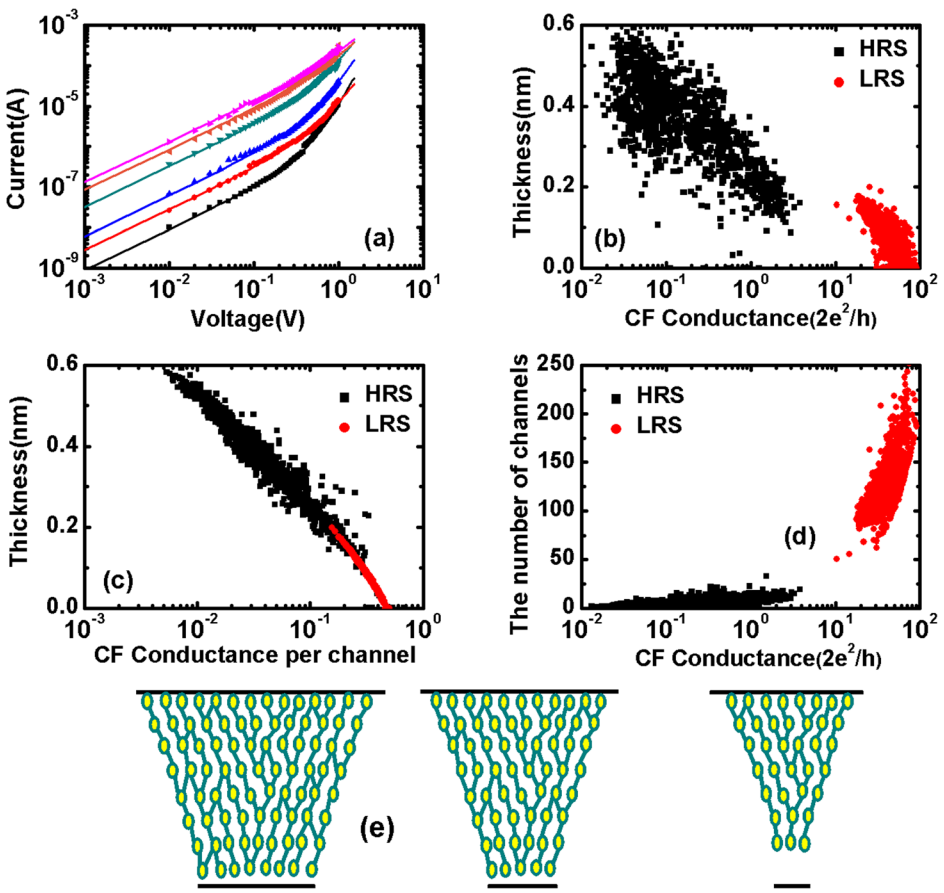

FIG. 6. Application of the QPC model to Pt/Ti/HfO_2/Pt structures operated under unipolar RS conditions. (a) Fitting of I-V to the QPC model in the HRS. Statistics of extracted QPC model parameters extracted from the fitting of 1250 I-V curves after the reset RVS in unipolar RS modes: (b) thickness of the gap versus CF conductance; and (c) gap thickness versus conductance per channel. (d) The number of conducting channels versus CF conductance. (e) The evolution of CF structure in unipolar experiments.

130 in the LRS and 5 in the HRS. Therefore, the number of conductance channels decreases and a gap is opened that is about two re-oxidized vacancies from the LRS to the HRS. Finally, Fig. 6(e) schematically shows the evolution of the microscopic structure of the CF in Pt/Ti/HfO_2/Pt devices when the evolution from the LRS to the HRS during unipolar RS mode. In the LRS, there are many conductive filaments and very small thickness gap between two electrodes. Then, the CF is narrowing and opening about two re-oxidized vacancies gap in the HRS.

IV. CONCLUSIONS

The QPC model has been applied to a thorough statistical study of resistance switching in RRAM devices. The fitting of I-V characteristic is excellent in both HRS and the LRS for two different structures in three RS modes. After reformulating the QPC model for CF conduction by coupling it to the results of *ab-initio* simulations of oxygen vacancy paths, we can obtain indirect information about the microscopic structure of the CF in both Pt/HfO_2/Pt and Pt/Ti/HfO_2/Pt devices. For Pt/HfO_2/Pt devices, the CF is symmetric with the most constrictive part likely located in the center of the CF. Starting from a very wide CF in the LRS, the width of the CF in its narrowest part reduces to a limit where only one or few oxygen vacancy paths connect the electrodes. This stage is followed by the opening of a gap that the thickness of the most conductive single vacancy path determines the CF conductance in the HRS. For Pt/Ti/HfO_2/Pt devices, the CF is strongly asymmetric, with the narrowest constrictive part near the bottom interface. The CF is deduced to be conical with the tip contacting the bottom electrode being the active region during switching. The Ti film is believed to act as an oxygen extraction layer and to introduce a high density of oxygen vacancies in the HfO_2. In the LRS, the CF area is rather large and there is one re-oxidized vacancy gap for bipolar RS mode, then the gap increases to two or three vacancies and the CF is narrower than the LRS. For unipolar RS mode, the number of paths in the HRS is much less than bipolar RS mode, this is to say, the unipolar RS mode is more effective than bipolar RS mode. The obtained results have revealed significant differences in the properties of the CF in these two types of devices. This is consistent with the expected differences in the concentration profile of oxygen vacancies due to the presence/absence of an oxygen extraction layer.

ACKNOWLEDGMENTS

A part of the work has been performed in the project PANACHE, co-funded by grants from Spain (Project Nos. PCIN2013-076 and TEC2012-32305 of the Spanish Ministerio de Econonía y Competitividad), France, and the ENIAC Joint Undertaking. Project No. TEC2012-32305 was co-funded by the EU under the FEDER program. S. Long and M. Liu acknowledge the funding support of the Ministry of Science and Technology of China under Grant Nos. 2010CB934200 and 2011CBA00602 and the National Natural Science Foundation of China under Grant Nos. 61221004 and 61274091. Jordi Suñé also acknowledges the ICREA Academia award. Devices and data have been obtained in the frame of internal CEA-LETI research programs.

[1]R. Waser and M. Aono, Nature Mater. **6**, 833 (2007).
[2]A. Sawa, Mater. Today **11**, 28 (2008).
[3]R. Waser, R. Dittmann, G. Staikov, and K. Szot, Adv. Mater. **21**, 2632 (2009).
[4]D. Ielmini, R. Bruchhaus, and R. Waser, Phase Transitions **84**, 570 (2011).
[5]J. J. Yang, D. B. Strukov, and D. R. Stewart, Nat. Nanotechnol. **8**, 13 (2013).
[6]D. S. Jeong, R. Thomas, R. S. Katiyar, J. F. Scott, H. Kohlstedt, A. Petraru, and C. S. Hwang, Rep. Prog. Phys. **75**, 076502 (2012).
[7]K. M. Kim, D. S. Jeong, and C. S. Hwang, Nanotechnology **22**, 254002 (2011).
[8]H.-S. P. Wong, H.-Y. Lee, S. Yu, Y.-S. Chen, Y. Wu, P.-S. Chen, B. Lee, F. T. Chen, and M.-J. Tsai, Proc. IEEE **100**, 1951 (2012).
[9]S. C. Chae, J. S. Lee, S. Kim, S. B. Lee, S. H. Chang, C. Liu, B. Kahng, H. Shin, D.-W. Kim, C. U. Jung, S. Seo, M.-J. Lee, and T. W. Noh, Adv. Mater. **20**, 1154 (2008).
[10]Y. C. Yang, P. Gao, S. Gaba, T. Chang, X. Pan, and W. Lu, Nat. Commun. **3**, 732 (2012).
[11]C. Cagli, F. Nardi, and D. Ielmini, IEEE Trans. Electron Devices **56**, 1712 (2009).
[12]S. Long, Q. Liu, H. Lv, Y. Li, Y. Wang, S. Zhang, W. Lian, K. Zhang, M. Waong, H. Xie, and M. Liu, Appl. Phys. A **102**, 915 (2011).
[13]W. Guan, M. Liu, S. Long, Q. Liu, and W. Wang, Appl. Phys. Lett. **93**, 223506 (2008).
[14]S. Yu and H.-S. P. Wong, IEEE Trans. Electron Devices **58**, 1352 (2011).
[15]S. Lavizzari, D. Ielmini, and A. L. Lacaita, IEEE Trans. Electron Devices **57**, 3257 (2010).
[16]J. S. Lee, S. B. Lee, S. H. Chang, L. G. Gao, B. S. Kang, M.-J. Lee, C. J. Kim, T. W. Noh, and B. Kahng, Phys. Rev. Lett. **105**, 205701 (2010).
[17]H. D. Lee, B. Magyari-Köpe, and Y. Nishi, Phys. Rev. B **81**, 193202 (2010).
[18]S. Yu, X. Guan, and H.-S. P. Wong, Appl. Phys. Lett. **99**, 063507 (2011).
[19]D. Ielmini, F. Nardi, and C. Cagli, Nanotechnology **22**, 254022 (2011).
[20]D. Ielmini, IEEE Trans. Electron Devices **58**, 4309 (2011).
[21]H. Y. Lee, P.-S. Chen, T.-Y. Wu, Y. S. Chen, F. Chen, C.-C. Wang, P.-J. Tzeng, C. H. Lin, M.-J. Tsai, and C. Lien, IEEE Electron Device Lett. **30**, 703 (2009).
[22]J. Suñé, E. Miranda, M. Nafria, and X. Aymerich, IEEE Tech. Dig. – Int. Electron Devices Meet. **1998**, 191.
[23]J. Suñé and E. Miranda, IEEE Tech. Dig. – Int. Electron Devices Meet. **2000**, 533.
[24]J. R. Jameson, N. Gilbert, F. Koushan, J. Saenz, J. Wang, S. Hollmer, M. Kozicki, and N. Derhacobian, IEEE Electron Device Lett. **33**, 257 (2012).
[25]X. Zhu, W. Su, Y. Liu, B. Hu, L. Pan, W. Lu, J. Zhang, and R.-W. Li, Adv. Mater. **24**, 3941 (2012).
[26]S. Tappertzhofen, I. Valov, and R. Waser, Nanotechnology **23**, 145703 (2012).
[27]S. Long, X. Lian, C. Cagli, X. Cartoixà, R. Rurali, E. Miranda, D. Jiménez, L. Perniola, M. Liu, and J. Suñé, Appl. Phys. Lett. **102**, 183505 (2013).
[28]X. Lian, E. Miranda, S. Long, L. Perniola, M. Liu, and J. Suñé, in *ULIS* (2013), pp. 161–163.
[29]X. Lian, E. Miranda, S. Long, L. Perniola, M. Liu, and J. Suñé, Solid-State Electron. **98**, 38 (2014).
[30]E. Miranda, C. Walczyk, C. Wenger, and T. Schroeder, IEEE Electron Device Lett. **31**, 609 (2010).
[31]R. Degraeve, Ph. Roussel, L. Goux, D. Wouters, J. Kittl, L. Altimine, M. Jurczak, and G. Groseneken, IEEE Tech. Dig. – Int. Electron Devices Meet. **2010**, 632.
[32]E. Miranda, S. Kano, C. Dou, K. Kakushima, J. Suñé, and H. Iwai, Appl. Phys. Lett. **101**, 012910 (2012).
[33]J. M. Soler, E. Artacho, J. D. Gale, A. García, J. Junquera, P. Ordejón, and D. Sánchez-Portal, J. Phys.: Condens. Matter **14**, 2745 (2002).
[34]X. Zhao and D. Vanderbilt, Phys. Rev. B **65**, 233106 (2002).
[35]H. J. Monkhorst and J. D. Pack, Phys. Rev. B **13**, 5188 (1976).
[36]S.-G. Park, B. Magyari-Köpe, and Y. Nishi, Phys. Rev. B **82**, 115109 (2010).
[37]X. Cartoixà, R. Rurali, and J. Suñé, Phys. Rev. B **86**, 165445 (2012).
[38]X. Lian, S. Long, C. Cagli, J. Buckley, E. Miranda, M. Liu, and J. Suñé, in *ULIS* (2012), pp. 101–104.

[39]S. Datta, *Electronic Transport in Mesoscopic Systems* (Cambridge University Press, 1997).
[40]M. Büttiker, Phys. Rev. B **41**, 7906 (1990).
[41]E. N. Bogachek, A. G. Scherbakov, and U. Landman, Phys. Rev. B **56**, 1065 (1997).
[42]E. Miranda and J. Suñé, in *Annual Proceedings-Reliability Physics (Symposium)* (2001), pp. 367–379.
[43]U. Russo, D. Ielmini, C. Cagli, A. L. Lacaita, S. Spiga, C. Wiemer, M. Perego, and M. Fanciulli, IEEE Tech. Dig. – Int. Electron Devices Meet. **2007**, 775.
[44]U. Russo, D. Ielmini, C. Cagli, and A. L. Lacaita, IEEE Trans. Electron Devices **56**, 193 (2009).
[45]D. C. Gilmer, G. Bersuker, S. Koveshnikov, M. Jo, A. Kalantarian, B. Butcher, R. Geer, Y. Nishi, P. D. Kirsch, and R. Jammy, in *Proceedings of IEEE International Memory Workshop* (2012), p. 978.